THE ASTROPHYSICAL JOURNAL, 376:214–222, 1991 July 20

A POWERFUL LOCAL SHEAR INSTABILITY IN WEAKLY MAGNETIZED DISKS. I. LINEAR ANALYSIS

STEVEN A. BALBUS AND JOHN F. HAWLEY
Virginia Institute for Theoretical Astronomy, Department of Astronomy, University of Virginia, P.O. Box 3818, Charlottesville, VA 22903
Received 1990 November 1; accepted 1991 January 16

ABSTRACT

In this paper and a companion work, we show that a broad class of astrophysical accretion disk is dynammically unstable to axisymmetric disturbances in the presence of a weak magnetic field. Because of the ubiquity of magnetic fields, this result bears upon gaseous differentially rotating systems quite generally. This work presents a linear analysis of the instability. (The companion work presents the results of nonlinear numerical simulations.) The instability is local and extremely powerful. The maximal growth rate is of order the angular rotation velocity and is *independent* of the strength of the magnetic field, provided only that the energy density in the field is less than the thermal energy density. Unstable axisymmetric disturbances require the presence of a poloidal field component, and are indifferent to the presence of a toroidal component. The instability also requires that the angular velocity be decreasing outward. In the absence of a powerful dissipation process, there are no other requirements for instability. Fluid motions associated with the instability directly generate both poloidal and toroidal field components. We discuss the physical interpretation of the instability in detail. Conditions under which saturation occurs are suggested. The *nonemergence* of the classical Rayleigh criterion for shear instability in the limit of vanishing field strength is noted and explained. The instability is sensitive neither to disk boundary conditions nor to the constituative fluid properties. Its existence precludes the possibility of internal (noncompressive) wave propagation in a disk. If present in astrophysical disks, the instability, which has the character of an interchange, is very likely to lead to generic and efficient angular momentum transport, thereby resolving an outstanding theoretical puzzle.

Subject headings: accretion — hydrodynamics — hydromagnetics — instabilities

1. INTRODUCTION

A long-standing challenge to the theory of accretion disks has been to show from first principles a mechanism capable of generating a turbulent viscosity, since the angular momentum transport resulting from the action of ordinary molecular viscosity is extremely inefficient (Pringle 1981). In this work and a companion paper (Hawley & Balbus 1991, hereafter II), we show that accretion disks are subject to a very powerful shearing instability mediated by a *weak* magnetic field of any plausible astrophysical strength. We suggest that this instability is of some relevance to understanding the origin of turbulent viscosity in accretion disks.

It is of course widely appreciated that magnetic fields can play an important role in accretion disk dynamics (e.g., Blandford 1989). In their seminal paper, Shakura & Sunyaev (1973) noted that magnetic turbulance could act as a viscous couple, but argued that nonlinear perturbations would be required to disrupt laminar flow. Magnetic fields have also been invoked, for example, as a source of coronal heating (Galeev, Rosner, & Vaiana 1979), and wind production (Blandford & Payne 1982). Despite the recognition of the importance of magnetic fields, stability analyses and wave propagation studies are nearly always gasdynamical in character. An important finding of this paper is that even an arbitrarily small magnetic field cannot be ignored when considering linear disturbances in accretion disks. Indeed, a weak magnetic field may be far more destabilizing than a strong one. The growth rate of the instability, which is of order the disk angular frequency, is considerably more rapid than any wave propagation time of interest. The nonlinear resolution of the instability is difficult to predict with any certainty, but a classical turbulent structure on scales from the disk scale height down to a dissipative reconnection length appears to be a viable and interesting possibility (II).

The instability has some extraordinary properties. It is present if a disk (1) is differentially rotating with a rate decreasing with distance from the center; and (2) has a weak (subthermal Alfvén speed) poloidal component. Remarkably, neither the growth rate of the most rapidly growing wavenumbers nor the stability criterion itself formally depend upon the magnetic field strength. However, the critical wavelength, longward of which instability sets in, is directly proportional to the magnetic field. (The wavelength of maximum growth is of the same order but slightly larger than the critical wavelength.) Thus, dissipational forces would ultimately become important as the field goes to zero; in the opposite limit, for a sufficiently large field, the critical wavelength will exceed the characteristic scale height of the disk. If nothing else intervenes, the latter will clearly be relevant to the nonlinear saturation of the instability. The essence of our results is that the *Rayleigh instability criterion of a negative radial gradient in specific angular momentum is largely irrelevant to gaseous astrophysical disks. Instead, the combination of a negative angular velocity radial gradient with almost any small seed field will lead to dynamical instability.* In the early stages of growth, the behavior of the evolving disturbances has the character of a classical interchange instability (II).

While all this may seem surprising, a related process was studied long ago by Chandrasekhar (1960). He considered the *global* stability of a vertically magnetized column of incompressible fluid undergoing Couette flow, and for a vanishingly small field found precisely the same instability criterion described above. In his paper, Chandrasekhar (1960) noted explicitly, and with some surprise, the nonemergence of the Rayleigh criterion in the vanishing field limit. Later, Fricke (1969) studied the local stability of

stellar differential rotation in the presence of a magnetic field, emphasizing the incompatibility of stellar isorotational configurations (Ferraro 1937) with dynamical stability. Fricke realized fully the connection between his own work and Chandrasekhar's (1960) investigation. The importance of these authors' findings to accretion disk theory seems to have gone unappreciated. Some of our formal results were first obtained by Fricke, but they are derived here in a much different physical context. For reasons that will be made clear below, the derivation and final form of the fundamental dispersion formula presented here are simpler than those in Fricke (1969).

At this point, it may be useful to emphasize what the instability is *not*. It is not a limiting form of a magnetic "swing amplifier" (Tagger et al. 1990), which involves the propagation of magnetoacoustic waves. It is not related to the magnetoacoustic instability discussed by Lynden-Bell (1966) and more recently by Elmegreen (1987) as a promoter of gravitational collapse in the spiral arm regions of disk galaxies. In this latter process, the disturbances are compressive, self-gravity is key, and although the magnetic field always destabilizes, growth rates depend directly on the strength of the field. The present instability is noncompressive, self-gravity is not involved, and the characteristic growth rate is (to reiterate) independent of the magnetic field strength.

Since the destabilization mechanism involved is insensitive both to the boundary conditions at the disk edge and to the constitutive relation for the gas, it is our belief that the instability constitutes the strongest evidence to date that accretion disks are in fact turbulent along the lines of the α-prescription (Shakura & Sunyaev 1973). The linear analysis gives an explicit picture of the underlying physics of the instability, and suggests the conditions under which it may saturate. In the absence of dissipation, this occurs when the Alfvén speed becomes of order the thermal velocity in the disk, at a critical wavelength on the order of the disk scale height. This is precisely the scale associated with angular momentum transport in an $\alpha \lesssim 1$ accretion disk. The presence of dissipative reconnection would lower α.

In this work, paper I of this series, our contributions are: (1) to show that the instability manifests itself locally under very general conditions; (2) to give a relatively simple derivation of the fundamental dispersion formula and stability criterion; (3) to provide a detailed explanation of the underlying physical cause; and (4) to present the limitations of the theory. In paper II, the nonlinear evolution is explored numerically using a two-dimensional magnetohydrodynamic simulation. The local analysis is presented in the next section, followed by an interpretation of the instability, a simple application, and finally some concluding remarks.

2. A SHEARING INSTABILITY IN A MAGNETIZED DISK

2.1. *The Instability in Brief*

While we present a discussion of the physical nature of the instability in § 2.5, let us understand the basic destabilization mechanism before embarking on a detailed calculation. Consider an outwardly displaced fluid element in a differentially rotating disk threaded by a vertical magnetic field. The fundamental point is that the element is elastically tethered by a magnetic field which is trying simultaneously to enforce rigid rotation (by resisting shearing), and to return the element back to its starting point (by resisting stretching). The latter is clearly stabilizing, but the first is the heart of the instability: the field is trying to force the element to rotate too fast for its new radial location. The excess centrifugal force drives the element still farther outward. At long wavelengths, the return force is weak, and destabilization wins. The presence of a finite vertical wavenumber in the disturbance is essential; there can be no axisymmetric instability otherwise. This allows fingers of high and low angular momentum fluid to interpenetrate. The instability is basically simple. It is a particularly virulent kind of viscous couple.

2.2 *Axisymmetric Dispersion Relation: $B_R = 0$*

Consider an axisymmetric accretion disk of finite vertical extent, not necessarily thin. Set up a standard cylindrical coordinate system (R, ϕ, z) with R being the perpendicular distance from the z-axis. We assume that the equilibrium angular velocity $\Omega(R)$ is constant on cylinders, by tall other flow variables may depend upon R and z if permitted by the magneto-fluid equations. A magnetic field is presumed to be present in the disk, weak enough that in the initially unperturbed state its effect is quite negligible. Differential rotation will cause the equilibrium field to acquire a helical structure, and the presence of a radial component of the magnetic field together with shear will cause the azimuthal component to grow linearly with time. This leads to no great difficulties, but let us nevertheless begin our study with the special case of vanishing radial field component, $B_R = 0$. We then return to treat the more general case by building on the results of this slightly artificial but highly illustrative example.

We denote the azimuthal field component $B_\phi(R, z)\hat{\boldsymbol{\phi}}$, and the vertical component $B_z(R)\hat{\boldsymbol{z}}$. (The notation $\hat{\boldsymbol{\phi}}$, etc. is used to denote a unit vector.) The basic dynamical equations are

$$\frac{d\ln\rho}{dt} + \nabla\cdot\boldsymbol{v} = 0\,, \tag{2.1a}$$

$$\frac{d\boldsymbol{v}}{dt} + \frac{1}{\rho}\nabla\left(P + \frac{B^2}{8\pi}\right) - \frac{1}{4\pi\rho}(\boldsymbol{B}\cdot\nabla)\boldsymbol{B} + \nabla\boldsymbol{\Phi} = 0\,, \tag{2.1b}$$

$$\frac{\partial\boldsymbol{B}}{\partial t} - \nabla\times(\boldsymbol{v}\times\boldsymbol{B}) = 0\,. \tag{2.1c}$$

The notation d/dt indicates the Lagrangian derivative and $\boldsymbol{\Phi}$ is the external gravitational potential. Others symbols have their usual meanings.

We consider axisymmetric large-wavenumber Eulerian perturbations with space-time dependence $e^{i(k_R R + k_z z - \omega t)}$. Subscripts refer to vector components. Fourier amplitudes of perturbed flow attributes are denoted as $\delta\rho$, δP, etc. We shall work in the Boussinesq approximation, which is appropriate for the noncompressive disturbances of interest. This eliminates magnetoacoustic waves from

consideration, and greatly simplifies the bookkeeping. When written out in component form and only the largest terms retained, the above set of seven equations becomes to linear order

$$k_R \delta v_R + k_z \delta v_z = 0 , \tag{2.2a}$$

$$-i\omega \delta v_R + \frac{ik_R}{\rho} \delta P - 2\Omega \delta v_\phi - \frac{\delta\rho}{\rho^2}\frac{\partial P}{\partial R} + \frac{ik_R}{4\pi\rho}(B_\phi \delta B_\phi + B_z \delta B_z) - \frac{ik_z}{4\pi\rho} B_z \delta B_R = 0 , \tag{2.2b}$$

$$-i\omega \delta v_z + \frac{ik_z \delta P}{\rho} - \frac{\delta\rho}{\rho^2}\frac{\partial P}{\partial z} + \frac{ik_z}{4\pi\rho} B_\phi \delta B_\phi = 0 , \tag{2.2c}$$

$$-i\omega \delta v_\phi + \delta v_R \frac{\kappa^2}{2\Omega} - ik_z B_z \frac{\delta B_\phi}{4\pi\rho} = 0 , \tag{2.2d}$$

$$-i\omega \delta B_R - ik_z B_z \delta v_R = 0 , \tag{2.2e}$$

$$-i\omega \delta B_z - ik_z B_z \delta v_z = 0 , \tag{2.2f}$$

$$-i\omega \delta B_\phi - \frac{d\Omega}{d\ln R} \delta B_R - ik_z B_z \delta v_\phi = 0 . \tag{2.2g}$$

In the above, Ω is the angular velocity, and κ^2 is the square of the epicyclic frequency,

$$\kappa^2 \equiv \frac{2\Omega}{R}\frac{d(R^2\Omega)}{dR} .$$

Note that equations (2.2e), (2.2f), and (2.2a) guarantee $\nabla \cdot \delta \boldsymbol{B} = 0$. To complete our set, we require the entropy for adiabatic perturbations in the Boussinesq approximation:

$$i\omega \frac{5}{3}\frac{\delta\rho}{\rho} + \delta v_z \frac{\partial \ln P\rho^{-5/3}}{\partial z} + \delta v_R \frac{\partial \ln P\rho^{-5/3}}{\partial R} = 0 . \tag{2.2h}$$

Our strategy is to eliminate δv_R everywhere by using equation (2.2a), use equations (2.2c)–(2.2h) to express all δ-quantities in terms of δv_z, and construct the dispersion relation from equation (2.2b). En route we find

$$\frac{\delta\rho}{\rho} = -\frac{3}{5i\omega}\delta v_z\left(\frac{\partial \ln P\rho^{-5/3}}{\partial z} - \frac{k_z}{k_R}\frac{\partial \ln P\rho^{-5/3}}{\partial R}\right), \tag{2.3a}$$

$$\frac{\delta P}{\rho} + \frac{B\phi\, \delta B_\phi}{4\pi\rho} = \frac{\delta v_z}{k_z}\left[\omega + \frac{3}{5\omega}\frac{1}{\rho}\frac{\partial P}{\partial z}\left(\frac{\partial \ln P\rho^{-5/3}}{\partial z} - \frac{k_z}{k_R}\frac{\partial \ln P\rho^{-5/3}}{\partial R}\right)\right], \tag{2.3b}$$

$$\delta v_R = -\frac{k_z}{k_R}\delta v_z , \tag{2.3c}$$

$$\delta v_\phi = \frac{\delta v_z}{i\omega}\frac{k_z}{k_R}\left(-\frac{\kappa^2}{2\Omega} + \frac{k_z^2 v_{Az}^2}{\omega^2}\frac{d\Omega}{d\ln R}\right)\left(1 - \frac{k_z^2 v_{Az}^2}{\omega^2}\right)^{-1} , \tag{2.3d}$$

$$\delta B_z = -\frac{k_z B_z}{\omega}\delta v_z , \tag{2.3e}$$

$$\delta B_R = \frac{k_z^2}{k_R} B_z \frac{\delta v_z}{\omega} , \tag{2.3f}$$

$$\delta B_\phi = 2\Omega \frac{B_z}{i\omega^2}\frac{k_z^2}{k_R}\left(1 - \frac{k_z^2 v_{Az}^2}{\omega^2}\right)^{-1}\delta v_z , \tag{2.3g}$$

where

$$v_{Az}^2 = \frac{B_z^2}{4\pi\rho} . \tag{2.4}$$

Combining equations (2.3a)–(2.3f) into equations (2.2b) yields the desired dispersion relation after rearranging and simplification:

$$\tilde{\omega}^4 + \frac{k_z^2}{k^2}\left[\frac{3}{5\rho}\left(\frac{k_R}{k_z}\frac{\partial P}{\partial z} - \frac{\partial P}{\partial R}\right)\left(\frac{k_R}{k_z}\frac{\partial \ln P\rho^{-5/3}}{\partial z} - \frac{\partial \ln P\rho^{-5/3}}{\partial R}\right) - \kappa^2\right]\tilde{\omega}^2 - 4\Omega^2\frac{k_z^4 v_{Az}^2}{k^2} = 0 , \tag{2.5}$$

where

$$\tilde{\omega}^2 \equiv \omega^2 - k_z^2 v_{Az}^2 , \tag{2.6a}$$

and

$$k^2 \equiv k_z^2 + k_R^2 . \tag{2.6b}$$

In this form, equation (2.5) reduces to the inviscid dispersion relation of Fricke (1969). Note that in contrast to the derivation presented by Fricke, our calculation includes both a toroidal and a poloidal field together. While the toroidal field drops out of the final dispersion relationship, the simultaneous consideration of *both* components is of importance in justifying the validity of the Boussinesq approximation. The pure toroidal field case considered by Fricke was considerably more restrictive in this regard. Additionally, we may simplify things a bit further by noting that

$$\frac{\partial P}{\partial R}\frac{\partial \ln P\rho^{-5/3}}{\partial z} = \frac{\partial P}{\partial z}\frac{\partial \ln P\rho^{-5/3}}{\partial R} , \tag{2.7}$$

which follows from the assumption of rotation on cylinders, or equivalently that isobaric and isochoric surfaces coincide. Then, defining

$$N_z^2 \equiv -\frac{3}{5\rho}\frac{\partial P}{\partial z}\frac{\partial \ln P\rho^{-5/3}}{\partial z} , \tag{2.8}$$

with an analogous expression for N_R^2, the final form of the dispersion relation becomes comparatively simple:

$$\frac{k^2}{k_z^2}\tilde{\omega}^4 - \left[\kappa^2 + \left(\frac{k_R}{k_z}N_z - N_R\right)^2\right]\tilde{\omega}^2 - 4\Omega^2 k_z^2 v_{Az}^2 = 0 . \tag{2.9}$$

The quantities N_z^2 and N_R^2 are pieces of the Brunt-Väisälä frequency:

$$N^2 = -\frac{3}{5\rho}(\nabla P)\cdot(\nabla \ln P\rho^{-5/3}) = N_z^2 + N_R^2 , \tag{2.10}$$

and should not be confused with vector components. Note that only the z-component of the magnetic field enters the dispersion relation, and that it is always multiplied by the wavenumber k_z. Thus, the importance of arbitrarily small magnetic fields is readily understood: significant magnetic tension forces can be generated at sufficiently small wavelengths. Another particularly useful way to think of this is to observe that in the *absence* of magnetic fields, there is no wavenumber scale in the problem: internal waves propagate with a frequency that depends only on wavenumber direction. The presence of a field establishes an inverse length scale for the wavenumbers: Ω/v_{Az}. By normalizing the components of $\boldsymbol{k}$ by this characteristic value, the field scales out of the problem. Only the value of the wavenumber relative to Ω/v_{Az} matters, not the value of the field strength directly.

There are two physical branches to the dispersion relation (2.9): the internal wave branch (mentioned above) which is present in the absence of a magnetic field, and a torsional wave branch which becomes unstable at sufficiently long wavelengths when a field is present. Tightly wound internal waves have been suggested as a means of angular momentum transport and dynamo activity in accretion disks (Vishniac & Diamond 1989; Vishniac, Jin, & Diamond 1990). But these studies assume that the magnetic field has a negligible effect on wave propagation properties, at least if the magnetic pressure is small compared with the thermal pressure. If any weak magnetic field is present in the disk, equation (2.9) indicates this assumption is incorrect. Even if the presence of the field did not destabilize the disk in a rotation time, the radial range over which internal waves could propagate would be severely curtailed by Alfvénic couplings. But of course the main point of this study is the surprisingly unstable nature of weakly magnetized disks. Indeed, in light of our results, it is very difficult to justify much of what has been taken for granted in field-amplification schemes. To cite one example, the simple linear (in time) build-up of an azimuthal field from a small radial field must proceed much differently in the presence of the instability (see § 2.4).

In what follows, we shall assume that both the epicyclic frequency and the Brunt-Väisälä frequency (and its "pieces") are real; this is sufficient to ensure that the nonmagnetized disk is stable to inviscid adiabatic perturbations.

2.3. *Stability Criterion*

It is elementary to show that $\tilde{\omega}^2$ (and thus ω^2) must always be real and a continuous function of its parameters in the dispersion relation (2.9). Hence, we may investigate the stability of the weakly magnetized disk by considering conditions in the neighborhood of $\omega^2 = 0$, or $\tilde{\omega}^2 = -k_z^2 v_{Az}^2$. In this limit, equation (2.9) may be written:

$$k_R^2(k_z^2 v_{Az}^2 + N_z^2) - 2k_R k_z N_R N_z + k_z^2\left(\frac{d\Omega^2}{d\ln R} + N_R^2 + k_z^2 v_{Az}^2\right) = 0 . \tag{2.11}$$

Regarded as a quadratic equation for k_R, equation (2.11) does not allow real solutions for k_R (thereby assuring stability since ω^2 could then not pass through zero), provided the discriminant is negative. This requirement may be expressed as

$$k_z^4 v_{Az}^4 + k_z^2 v_{Az}^2\left(N^2 + \frac{d\Omega^2}{d\ln R}\right) + N_z^2\frac{d\Omega^2}{d\ln R} > 0 \qquad \text{(STABILITY)} . \tag{2.12}$$

Recalling the assumption $N_z^2 > 0$, it is immediately apparent that inequality (2.12) can be satisfied for all nonvanishing k_z if and only if

$$\frac{d\Omega^2}{dR} \geq 0 \qquad \text{(STABILITY)} , \tag{2.13}$$

which is the stability criterion of interest. It is generally violated in astrophysical disks and will lead to instability for values of k_z less than the critical value obtained directly from equation (2.12):

$$(k_z)^2_{\rm crit} = \frac{1}{2v_{Az}^2}\left\{\left[\left(N^2 + \frac{d\Omega^2}{d\ln R}\right)^2 - 4N_z^2\frac{d\Omega^2}{d\ln R}\right]^{1/2} - \left[N^2 + \frac{d\Omega^2}{d\ln R}\right]\right\}. \tag{2.14a}$$

If the disk is rotating supersonically (i.e., $N_R^2 \ll N_z^2$, see § 2.8), or if the Brunt-Väisälä frequency N^2 is negligible, the critical wavenumber becomes

$$|(k_z)_{\rm crit}| = v_{Az}^{-1}\,|d\Omega^2/d\ln R|^{1/2}\,. \tag{2.14b}$$

If $N_z^2 = 0$, as in the disk midplane, then the stability criterion is

$$N_R^2 + \frac{d\Omega^2}{d\ln R} \geq 0 \qquad \text{(STABILITY)}\,, \tag{2.15}$$

which for supersonic velocities differs little from the criterion (2.13).

2.4. *The General Case:* $B_R \neq 0$

The presence of a radial field component leads to a growing B_ϕ in the unperturbed disk. The relevant field freezing equation is

$$\frac{\partial B_\phi}{\partial t} = B_R\frac{d\Omega}{d\ln R}\,. \tag{2.16a}$$

Since B_R does not change with time, the solution to equation (2.15) is

$$B_\phi(t) = B_\phi(0)\left[1 + \frac{B_R}{B_\phi(0)}\frac{d\Omega}{d\ln R}\,t\right]. \tag{2.16b}$$

Thus B_ϕ grows linearly with time. As long as the azimuthal component is dynamically weak, it does not affect the disturbances of interest here. The azimuthal field is completely absent from the dispersion formula (2.9), and the inclusion of a radial field does not change this result. It is true that the analog of equation (2.3b) with a radial field would now involve explicitly time-dependent terms in the unperturbed flow variables, but the approximation made in assuming a time dependence $e^{-i\omega t}$ is still valid to leading exponential order. (This may be formalized with WKB expansions in the temporal domain, but we shall avoid this digression.) It is a straightforward, if slightly tedious excercise to show that the general dispersion formula, in an obvious notation, is

$$\frac{k^2}{k_z^2}\,\tilde\omega^4 - \left[\kappa^2 + \left(\frac{k_R}{k_z}N_z - N_R\right)^2\right]\tilde\omega^2 - 4\Omega^2(\boldsymbol{k}\cdot\boldsymbol{v}_A)^2 = 0\,, \tag{2.17}$$

where now,

$$\tilde\omega^2 \equiv \omega^2 - (\boldsymbol{k}\cdot\boldsymbol{v}_A)^2\,. \tag{2.18}$$

We encounter no surprises here. As promised, to leading order B_ϕ is absent from equation (2.17), and ω is free of explicit time dependence. In an important sense, no generality is lost by considering only the special case $B_R = 0$. For a given wavenumber $\boldsymbol{k}$, equation (2.17) shows that any field geometry may be reduced to an equivalent pure z-field problem by choosing a new v_{Az} equal to $\boldsymbol{k}\cdot\boldsymbol{v}_A/k_z$.

The question of the stability of the disk may be approached by the methods of the previous section. One apparent complication is that the counterpart to equation (2.11)

$$k_R^2[(\boldsymbol{k}\cdot\boldsymbol{v}_A)^2 + N_z^2] - 2k_R k_z N_R N_Z + k_z^2\left[\frac{d\Omega^2}{d\ln R} + N_R^2 + (\boldsymbol{k}\cdot\boldsymbol{v}_A)^2\right] = 0\,, \tag{2.19}$$

no longer is a quadratic in k_R, it becomes a quartic. But to show the *necessity* of $d\Omega^2/dR \geq 0$ as a stability criterion, it suffices to consider only long wavelengths. Retaining only the lowest-order terms quadratic in the wavenumber components in equation (2.19) leads to a problem nearly identical to the one analyzed in § 2.3: if the inequality (2.13) is violated, long wavelengths are easily shown to be unstable. To show the *sufficiency* of the criterion we reason as follows. "Solve" equation (2.19) as a quadratic for k_R as though $\boldsymbol{k}\cdot\boldsymbol{v}_A$ were simply a parameter. One obtains not, of course, a true solution, but a self-consistency requirement. Assume that a real-valued k_R solution does exist, i.e., that the flow is unstable. Then the formal discriminant in the formal solution for k_R must be positive. But if $d\Omega^2/dR \geq 0$, it is easily shown that the discriminant is *always* negative for any real-valued k_R and k_z. There is *never* a self-consistent solution for k_R in this case, the flow is always stable. This proves the sufficiency of the stability requirement. The special case $N_z^2 = 0$ poses no additional difficulties beyond those noted in § 2.3.

The fact that $d\Omega^2/dR \geq 0$ guarantees stability fits in rather neatly with the well-known result that a system attains its minimum energy configuration when in a state of uniform rotation (Lynden-Bell & Pringle 1974). A Keplerian disk does not have this state accessible to it, but other systems (e.g., stellar interiors) do, and the instability will in these cases simply redistribute angular momentum outwards until such time as the minimum energy state is attained.

We conclude that the criteria (2.13) and (2.15) hold for arbitrary magnetic field geometry. Note that these criteria are not beholden to thin disk approximations, but are of relevance to any weakly magnetized differentially rotating system with $\Omega = \Omega(R)$.

2.5. *Another Look at the Physical Nature of the Instability*

The basic destabilizing mechanism was first discussed in § 2.1. It is appropriate at this point to reconsider the physical nature of the instability now that we have derived the dispersion relation.

Lurking in the field-free disk is a latent instability. It corresponds to an axisymmetric azimuthal displacement, and $\omega^2 = 0$ trivial disturbance. It is this mode that comes to life when a magnetic field, however, weak, is added to the disk. We return to the simple case of a vertical field. Consider two rings of disk material, half a wavelength apart along a field line. Without changing the velocity, a small azimuthal displacement is made in each of the rings. The first ring is displaced in the direction of the rotation, the second in the opposite direction. The sense of the resulting tension is to slow the first ring and speed up the second ring. The slowed ring will drop inward toward the axis to a location consistent with its reduced angular momentum. In doing so, radial field lines are created by the inward motion, and due to the presence of shear, these lines are azimuthally distorted. This in turn leads to azimuthal stresses, which in a normal disk (angular velocity decreasing outward) compete with restoring Alfénic torsional stresses over the fate of the ring. At long wavelengths, the torsional stresses lose, and the azimuthal stresses bleed the ring of angular momentum. This angular momentum is taken up by the second ring, which will continue to move out as the inner ring moves in. This is the essence of the instability.

The instability may also be approached profitably from the point of view of altered fluid element epicycles. We look not at the formal dispersion analysis of the last section, but at the details of the perturbed velocity structure on the verge of instability, $\omega^2 \to 0$. In this limit, equations (2.3d) and (2.3c) yield

$$\delta v_\phi = -\frac{\delta v_z}{i\omega}\frac{k_z}{k_R}\frac{d\Omega}{d\ln R} = -\frac{i}{\omega}\frac{d\Omega}{d\ln R}\,\delta v_R\,. \tag{2.20}$$

This value of δv_ϕ may also be obtained by balancing off the rightmost terms in equation (2.2g). A very simple interpretation of equation (2.20) follows from examining the Lagrangian perturbation of Ω, as opposed to the Eulerian δv_ϕ. Denote the radial displacement by ξ. Then $-i\omega\xi = \delta v_R$, and since $\delta v_\phi = R\,\delta\Omega$, equation (2.20) may be rewritten in terms of the Lagrangian perturbation $\Delta\Omega$:

$$R\,\delta\Omega + \xi R\frac{d\Omega}{dR} \equiv R\,\Delta\Omega = 0\,. \tag{2.21}$$

The content of equation (2.21) is obvious in hindsight. The Lagrangian perturbation of Ω must vanish at the critical value $\omega = 0$ since shear would otherwise use the generated δB_R to force an explicit time-dependence in δB_ϕ. No such restriction applies in the field-free case; the $\omega = 0$ solution does not require $\Delta\Omega$ to vanish. In contrast to a magnetized displacement, there is no tether to couple a dislocated fluid element to its equilibrium position. Indeed, it is well-known that the Lagrangian perturbation in specific angular momentum, not angular velocity, is the relevant vanishing quantity in a marginally stable unmagnetized disk. This fact leads straight to the Rayleigh criterion for stability. In our case, we may note that the excess centrifugal force of the radially displaced element is given by $-\xi\,d\Omega^2/d\ln R$ (using $\Delta\Omega = 0$), and the return force of the magnetic tension is $-(k_z v_{Az})^2\xi$ (taking $B_R = 0$, as before). Comparing the two forces leads to equation (2.14b) for the critical wavenumber.

2.6. *Validity of the Boussinesq Approximation*

The derivations of the dispersion formulae (2.9) and (2.17) were considerably eased by the use of the Boussinesq approximation. It ought to be checked.

The approximation consists of setting $\delta P = 0$ in all equations but the equation of motion. This zero compressibility requirement means that $\omega\,\delta\rho/\rho$ is ignored in comparison with the velocity terms in the mass conservation equation. This is easily justified with the help of equation (2.3a). More interesting is the neglect of $\delta P/P$ compared with $\delta\rho/\rho$ in the energy equation. The largest terms in equation (2.3b) imply

$$\frac{\delta P}{P} \sim \frac{B_\phi\,\delta B_\phi}{4\pi\rho c^2}\,, \tag{2.22}$$

where c is the isothermal sound speed. At wavelengths of interest, $\boldsymbol{k}\cdot\boldsymbol{v}_A \sim \Omega$ and $\omega \sim \Omega$. Using these relations and equation (2.3g) for δB_ϕ, we find that the above gives

$$\frac{\delta P}{P} \sim \left(\frac{v_{A\phi}}{c}\right)\left(\frac{k_z}{k_R}\right)\frac{\delta v_z}{c}\,, \tag{2.23}$$

where

$$v_{A\phi}^2 \equiv \frac{B_\phi^2}{4\pi\rho}\,.$$

Noting equation (2.3a) for $\delta\rho/\rho$, we conclude that the Boussinesq approximation is satisfied for $v_{A\phi}/c \ll 1$, with the apparent restriction that the ratio k_z/k_R not be too large. However, even in the limit $k_R \to 0$, the Boussinesq approximation does not lead to difficulties. This is because while $\delta P/P$ is now no longer negligible compared with $\delta\rho/\rho$, the latter quantity itself becomes extremely small, and buoyant forces are altogether unimportant. Physically, this case corresponds to motion in z = constant planes, so buoyant forces are absent. These are in fact, the most unstable local modes. Thus, the only restriction required to satisfy the

Boussinesq approximation is a subthermal azimuthal field. Numerical simulations (II) show that the instability remains quite vigorous and insensitive to compressional effects well into the nonlinear regime.

Fricke (1969) found a far more restrictive criterion for the validity of the Boussinesq approximation for a *pure* toroidal field (see his equation [24]). This is because the absence of a poloidal field component precludes the possibility of an Alfvénic response for an axisymmetric displacement.

2.7. *Validity of Ignoring Dissipation: Minimum Required Field Strengths*

How small can $|\boldsymbol{B}|$ become before the critical wavelength is so small that dissipational processes are important? To answer this, we consider a generalized diffusion coefficient χ (cm^2 s^{-1}). On dimensional grounds, the condition that damping be unimportant will typically be $\chi k_z^2/\Omega \ll 1$. Setting $k_z^2 = 3\Omega^2/v_{Az}^2$, its critical value in a Keplerian disk, we may write the restriction as

$$\frac{3\Omega\chi}{v_{Az}^2} \ll 1 . \tag{2.24}$$

Consider first the effects of finite resistivity. Then χ is given in cgs units by

$$\chi = \frac{5.1 \times 10^{12}}{T^{3/2}} \left(\frac{\ln\Lambda}{10}\right), \tag{2.25}$$

where $\ln\Lambda$ is the usual Coulomb logarithm (Spitzer 1962). In this case, the condition (2.24) may be expressed as a restriction of the plasma $\beta \equiv 8\pi\rho c^2/B^2$:

$$\beta \ll 1.6 \times 10^{10} T_4^{5/2} R_{12}^{3/2} \left(\frac{M_\odot}{M}\right)^{1/2} \left(\frac{10}{\ln\Lambda}\right), \tag{2.26}$$

where T_4 is the disk temperature in units of 10^4 K, R_{12} is the disk radius in units of 10^{12} cm, and $M/M_\odot$ is the central mass in solar units. We have assumed a Keplerian value for Ω. Clearly there is room to consider quite weak fields before finite resistivity effects are important in any astrophysical disk system.

As another example, we consider thermal conductivity. (Both the wavenumber $\boldsymbol{k}$ and the effective conduction are coupled to the direction along the field line.) The equivalent diffusion coefficient χ is of order $\kappa T/P$, where κ is the Spitzer (1962) conductivity, given in cgs units by

$$\kappa = 1.84 \times 10^{-6} \left(\frac{10}{\ln\Lambda}\right) T^{5/2}. \tag{2.27}$$

In this case, it is more convenient to directly calculate a lower limit to the magnetic field, since this quantity is independent of the disk density. Using the restriction (2.24), we find

$$B_z \gg 2.4 \times 10^{-4} T_4^{5/4} \left(\frac{M}{M_\odot}\right)^{1/4} R_{12}^{-3/4} \left(\frac{10}{\ln\Lambda}\right)^{1/2} \text{G}. \tag{2.28}$$

This represents a very small field indeed for most applications (see e.g., Blandford 1989).

2.8. *Isothermal Thin Keplerian Disk*

As a specific example, let us consider a thin, isothermal, Keplerian disk. The equations of vertical hydrostatic equilibrium is (e.g., Pringle 1981)

$$c^2 \frac{\partial \ln\rho}{\partial z} = -\frac{GMz}{R^3} = -\Omega^2 z , \tag{2.29}$$

where G is the gravitational constant and M is the central mass. Since c is assumed to be constant,

$$\rho = \rho(R) \exp\left(-z^2\Omega^2/2c^2\right) \equiv \rho(R) \exp\left(-z^2/H^2\right), \tag{2.30}$$

which defines the scale height H. At $z = H$ it follows from equations (2.8) and (2.29) that $N_z^2 = 0.8\Omega^2$. With the Keplerian law $\kappa^2 = \Omega^2$ and N_R^2 rather arbitrarily set to $0.01N_z^2$, the unstable root of the dispersion relation (2.9) is pictured in the three-dimensional plot shown in Figure 1*a*. We have made use of the natural scaling for this problem, with each grid mark corresponding to 0.1 wavenumber units, Ω/v_{Az}. For clarity, $-\omega^2$ is plotted, so instabilities appear as upward projections. By way of contrast, we show in Figure 1*b* the dispersion relation for a disk with $\kappa^2 = 5\Omega^2$, corresponding to an outwardly increasing shear. In Figure 1*c* a cross section through the maximum of ω^2 is plotted. The largest growth rates are approximately 0.75Ω. This implies a millionfold increase in amplitudes in less than three rotation periods!

It is of interest to relate the ratio $\lambda_{\text{crit}}/2H$ (the critical wavelength over disk thickness) to the magnetic field strength. For a thin isothermal Keplerian disk we have

$$\frac{v_{Az}}{c} = \frac{\sqrt{6}}{\pi} \frac{\lambda_{\text{crit}}}{2H}, \tag{2.31}$$

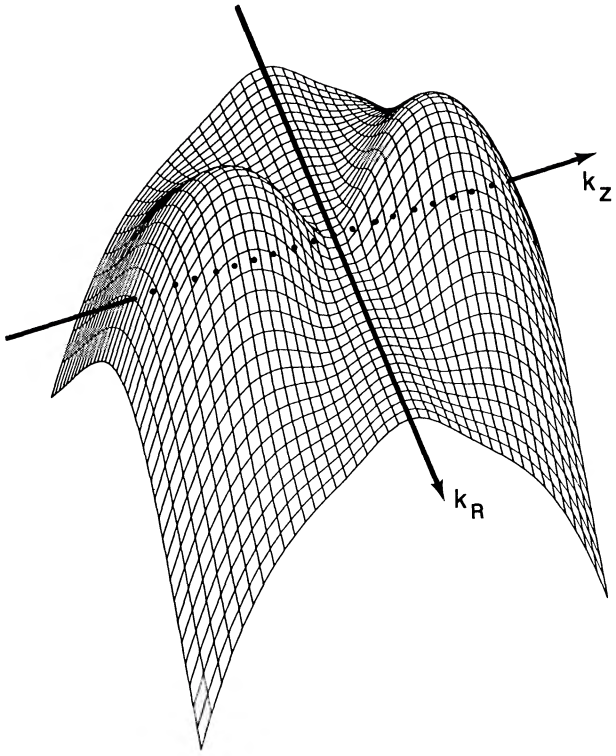

FIG. 1*a*

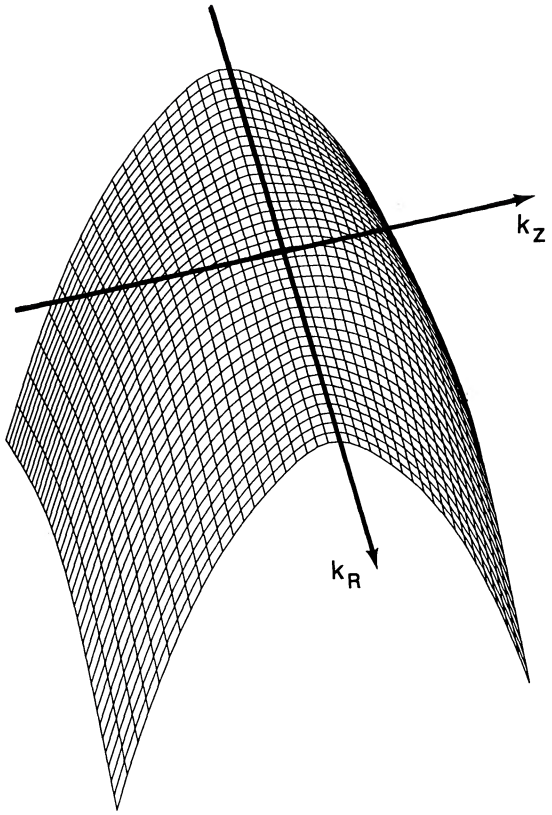

FIG. 1*b*

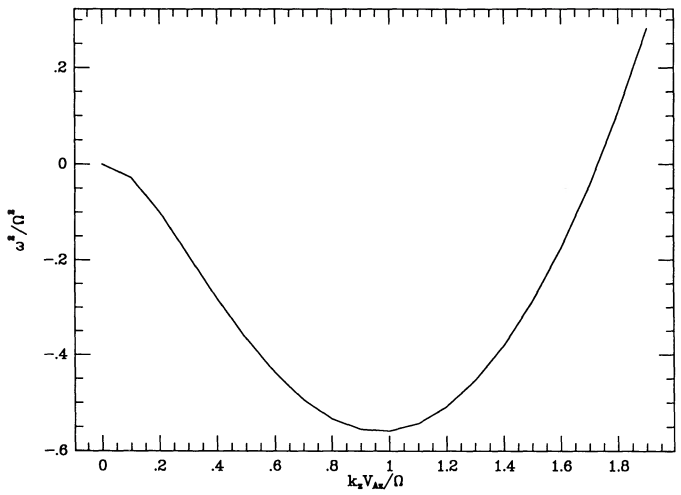

FIG. 1*c*

FIG. 1.—(*a*) Three-dimensional plot of the unstable branch of the dispersion relation (2.9). Relative values of $-\omega^2$ are plotted in the $k_R k_z$ plane for a thin isothermal Keplerian disk, with Brunt-Väisälä frequencies $N_z^2 = 0.8\Omega^2$ and $N_R^2 = 0.008\Omega^2$. Wavenumber values extend from -2 to 1.9 in units of Ω/v_{Az}. Grid marks are 0.1 units apart. The mounds represent regions of instability. (*b*) Same as Fig. 1*a*, but with an epicyclic frequency taken to be $5\Omega^2$ to produce an increasing outward angular velocity curve. The disk is clearly stable. (*c*) Plot of ω^2 through the region of maximum instability corresponding to $k_R = 0$.

or in terms of an effective plasma $\beta \equiv 8\pi\rho c^2/B_z^2$,

$$\beta = \frac{\pi^2}{3}\left(\frac{\lambda_{\rm crit}}{2H}\right)^{-2}. \tag{2.32}$$

We thus expect the instability to cease if the value of β drops below ~ 3.

3. CONCLUSIONS

We have shown that weakly magnetized accretion disks are subject to a powerful, axisymmetric shearing instability. The stability criteria (2.13) and (2.15) apply to any differentially rotating system with $\Omega = \Omega(R)$. The dispersion relation (2.9) indicates that the most rapidly growing wavenumbers in a thin disk have growth rates of about 0.75Ω. This is very rapid indeed—a factor of 10^6 in less than three rotation periods. The growth rate is independent of the strength of the magnetic field, perhaps the most startling finding of this work. If this instability is as robust as it appears to be, its importance lies in the generality of its applicability as well as its strength. The criterion for instability is simply a decreasing outward angular velocity law and the presence of a weak poloidal field component. Small-scale structure in a weak field does not seem to suppress the instability, a point we address in Paper II.

The most important consequence of the instability is that the mechanism behind a generic means of transport in accretion disks has been elucidated. The underlying cause of turbulent structure in accretion disks stems from the tendency of a weak magnetic field to try to enforce corotation on displaced fluid elements, a behavior which results in excess centrifugal force at larger radii, and a deficiency at smaller radii. When restoring forces are not able to compensate, displaced fluid elements are driven away from their equilibrium positions, leading to substantial angular momentum transport.

In this paper, we have not addressed the nature of nonaxisymmetric disturbances, nor have we gone beyond linear theory. The former clearly must be addressed before one can be certain about the presence of self-sustaining dynamo activity. As regards the latter, paper II of this series presents some nonlinear two-dimensional results in some simple disk representations. But largely because the instability *is* so powerful and produces large radial displacements, it has not been possible to run the simulations long enough to see saturation effects. Thus the ultimate nonlinear resolution of the instability is presently a topic for speculation. We see two categories of outcomes.

The first possibility is that the magnetic field will be built up to the point where the minimum critical wavelength exceeds the disk scale height. This occurs when the Alfvén and sound speeds are comparable, and leaves the magnetic field in a dynamically important and active state, but no longer prone to the shearing instability. The second possibility is that reconnection dissipates the growing field as structure cascades to ever smaller scales. The field never gets so large as to shut the instability off, but instead maintains a growth rate that counterbalances the dissipation at the smallest scales. This is of course the classical description of a turbulent cascade. In either case, a simple laminar disk is not a possibility. On the other hand, in both cases one would expect that the coherence length relevant to disk transport will be set by magnetically regulated turbulence, leading to the sort of picture put forward long ago by Shakura & Sunyaev (1973).

It is a pleasure to acknowledge the advice and encouragement of J. Binney, R. Blandford, J. Goodman, J. Pringle, and F. Shu. This research was supported by NSF grants AST 88-20293 and PHY 88-02747, and NASA grants NAGW-1510 and NAGW-764.

REFERENCES

Blandford, R. D. 1989, in Theory of Accretion Disks, ed. F. Meyer, W. J. Duschl, J. Frank, & E. Meyer-Hofmeister (Dordrecht: Kluwer), p. 35
Blandford, R. D., & Payne, D. G. 1982, MNRAS, 199, 883
Chandrasekhar, S. 1960, Proc. Nat. Acad. Sci., 46, 53
Elmegreen, B. G. 1987, ApJ, 312, 626
Ferraro, V. C. A. 1937, MNRAS, 97, 458
Fricke, K. 1969, A&A, 1, 388
Galeev, A., Rosner, R., & Vaiana, G. S. 1979, ApJ, 229, 318
Hawley, J. F., & Balbus, S. A. 1991, ApJ, 376, 223 (II)
Lynden-Bell, D. 1986, Observatory, 86, 57
Lynden-Bell, D., & Pringle, J. E. 1974, MNRAS, 168, 603
Pringle, J. E. 1981, ARA&A, 19, 137
Shakura, N. I., & Sunyaev, R. A. 1973, A&A, 24, 337
Spitzer, L. 1962, Physics of Fully Ionized Gases (New York: Wiley)
Tagger, M., Henriksen, R. N., Sygnet, J. F., & Pellat, R. 1990, ApJ, 353, 654
Vishniac, E. T., & Diamond, P. 1989, ApJ, 347, 447
Vishniac, E. T., Jin, L., & Diamond, P. H. 1990, ApJ, 365, 648.

THE ASTROPHYSICAL JOURNAL, 376:223–233, 1991 July 20

A POWERFUL LOCAL SHEAR INSTABILITY IN WEAKLY MAGNETIZED DISKS. II. NONLINEAR EVOLUTION

JOHN F. HAWLEY AND STEVEN A. BALBUS
Virginia Institute for Theoretical Astronomy, Department of Astronomy, University of Virginia, PO Box 3818, Charlottesville, VA 22903
Received November 1, 1990; accepted 1991 January 16

ABSTRACT

We consider the dynamical evolution of an accretion disk undergoing Keplerian shear flow in the presence of a weak magnetic field. A linear perturbation analysis presented in a companion paper shows that such a flow is dynamically unstable; here we consider some nonlinear consequences of this instability. We solve the equations of compressible magnetohydrodynamics using a two-dimensional finite-difference code. The Keplerian disk is threaded with a weak magnetic field that has a magnetic energy density much less than the thermal pressure. When perturbations are small, the numerical results are consistent with linear perturbation theory. We demonstrate the scaling relation between the instability's wavenumber and the Alfvén velocity that was found in the companion paper, and confirm that the maximum growth rate is independent of magnetic field strength. Neither compressibility nor the presence of toroidal field have a significant effect on the evolution of unstable modes. The most important dynamic effect is the redistribution of angular momentum leading to a strong interchange instability. The resulting radial motions produce field geometries that are conducive to reconnection, suggesting a possible mechanism for mode saturation. Even for very weak fields, whose most unstable wavelengths are small, nonlinear evolution results in the growth of structure on large scales. Total magnetic field energy increases by about one order of magnitude over the course of the simulations.

Subject headings: hydromagnetics — instabilities — stars: accretion

1. INTRODUCTION

In paper I (Balbus & Hawley 1991) we present a linear stability analysis for an accretion disk with magnetic field. We obtain the remarkable result that the presence of weak magnetic fields leads to a powerful local shearing instability. This result suggests that the full magnetohydrodynamic (MHD) equations must be solved when studying accretion disks, even for field strengths traditionally considered to be negligible. It has long been thought that a weak field will grow by shearing in an accretion disk, and that moderate strength fields can transfer angular momentum between fluid elements, possibly serving as a viscosity. It is clear that strong fields, with an energy density on order the thermal energy density, can significantly affect the disk, notably through magnetic buoyancy instabilities. However it now appears that field-disk interactions are dominated by a dynamical *instability* that inevitably results in exponentially growing magnetic fields and rapid angular momentum transfer. While idealized unmagnetized disks are extremely stable, astrophysical disks must be violently unstable, and the Rayleigh stability criterion is largely irrelevant. The existence of this instability is strong evidence for the oft-made assumption that accretion disks are turbulent.

In this paper we extend the linear analysis of paper I by carrying out numerical MHD simulations. Our goals are twofold. First, we wish to make the physical nature of the instability more palpable. Second, we seek some understanding of the nonlinear consequences of this instability through extended numerical stimulation. While there have been some recent MHD simulations of accretion disks, these have not explored the region of parameter space where this instability is operative. For example, the Parker instability has been studied by Matsumoto *et al.* (1990), but the initial magnetic energy density was on order of the thermal energy density, and—more significantly—angular momentum was neglected. Shibata & Uchida (1989) and Norman & Stone (1990) have simulated magnetically driven winds from disks, but in these studies the initial disk was not in equilibrium (it was sub-Keplerian), and was threaded with a strong magnetic field with an energy density in excess of the thermal energy density. Studies such as these have shown some dynamical effects of *strong* magnetic fields in accretion disks. However, as we have emphasized, *weak* magnetic fields are themselves of great importance and cannot be neglected.

In this work we concentrate on a simple section of a Keplerian disk threaded by a vertical magnetic field. The details of this model are described in § 2.1. The relation between the present work and the results of paper I is made explicit in § 2.2. The numerical techniques and diagnostics are outlined in § 2.3, and the results of the simulations are presented in § 3. These include a systematic investigation of the consequences of various initial field strengths, plus specific tests of other physical effects such as the effects of compressibility and a nonzero initial toroidal field. We present our conclusions in § 4.

2. PROBLEM CONFIGURATION AND NUMERICAL TECHNIQUE

2.1. *The Initial Model*

Since our aim in this paper is to provide a clear elucidation of the basic physics of the magnetic instability, we choose a particularly simple initial state. We consider a small region within a Keplerian flow in cylindrical coordinates, effectively reducing the accretion disk to a Keplerian cylindrical Couette flow. The grid is centered on R and extends in radius from $R - a$ to $R + a$ with a vertical thickness of a. We assume purely radial gravitational and centrifugal forces; there are no vertical pressure or density gradients. The assumption of

Keplerian flow means that gravitational and centrifugal forces are initially in radial balance. The angular velocity Ω is the Keplerian value at R. Pressure and density are taken to be constant throughout the box. Most, but not all of the simulations use an ideal gas equation of state with $\gamma = 5/3$. For simplicity, we use periodic boundary conditions on z and reflecting boundary conditions on the radial walls of the box.

These initial conditions are an acceptable representation of an accretion disk so long as the numerical grid is a small region centered about the disk's midplane. Self-consistency requires the grid scale a to be much less than R, the radial distance from the central gravitating mass, and H, the vertical scale-height of the disk at R. For comparison, an isothermal Keplerian disk has a vertical scale-height that is related to the sound speed c and the angular velocity Ω by

$$H^2 \sim 2c^2/\Omega^2 . \tag{2.1}$$

The physics of this ideal MHD simulation is scale-free. In the absence of forces in the z direction, the physically important length and time scales are set by Ω, the periodicity length in the z direction, here chosen to be equal to a, and the poloidal Alfvén speed v_A. The essential parameters are the ratios c/Ω and v_A/Ω. For convenience we set $GM = 1$ and center the grid at $R = 100$; this makes the Keplerian angular velocity at that point equal to 10^{-3}. Again for convenience we take $\rho = 1$, and choose the gas pressure $P = 10^{-5}$. Thus the ratio of the isothermal sound speed to the angular velocity at R is 10, giving a scale-height $H \sim 14$. For the simulation domain we choose a vertical thickness of $a = 1$ so that the simulation grid can be regarded self-consistently as a small region centered around R with a periodicity length in z that is a fraction of H.

We investigate the evolution of the magnetic instability by placing weak magnetic fields onto this hydrodynamically stable initial model. For most of the simulations we begin with a uniform z-field of finite radial extent, placed in the center of the grid. The magnetic field is set by choosing β_z, the ratio of gas to poloidal magnetic pressure,

$$\beta_z = \frac{P}{(B_z^2/8\pi)} . \tag{2.2}$$

When desired, we add a uniform toroidal field, similarly parameterized by β_ϕ. We have examined several initial field configurations.

2.2. *Connection with Linear Theory*

In paper I we show that the instability does not depend directly on the field strength, but only on the product of the poloidal Alfvén speed v_A over the angular velocity times the physical wavenumber. It is useful to define a normalized vector wavenumber parameter q that makes this explicit, writing

$$q_i = k_i v_A/\Omega , \tag{2.3}$$

where i can be either R or z.

In the numerical simulations we do not know *a priori* which wavevector $\boldsymbol{k}$ will emerge. The unstable modes that develop will be influenced by the grid size, the boundary conditions, and the initial field and perturbation. As a guideline, however, we can compute growth rates and wavelengths for a variety of wavenumbers scaled in terms of the periodicity length of the grid. Since we are considering the idealized case of a Keplerian distribution of angular velocity in a constant density and pressure background, the linear perturbation results of paper I can be written in a very simple form. The growth rate obtained from linear theory, after setting the Brunt-Väisälä frequency to zero, is found to be (eq. [2.9] of paper I)

$$\frac{\omega^2}{\Omega^2} = q_z^2\left\{1 - \frac{8}{[\kappa^2/\Omega^2 + (\kappa^4/\Omega^4 + 16\, q^2)^{1/2}]}\right\} , \tag{2.4}$$

where $q^2 = q_z^2 + q_R^2$, and the term κ is the epicyclic frequency; for a Keplerian disk $\kappa/\Omega = 1$. From equation (2.4) we see that the shortest unstable wavelength has $q^2 = 3$. By setting this critical wavelength equal to the periodicity length in the numerical grid, $\lambda_{\rm crit} = a = 1$, we find that $\beta_z = 266$ corresponds to the maximum field strength for which the instability should be present. The mode with wavenumbers $q_z = 1$, $q_R = 0$ has the maximum linear growth rate ($=0.75\Omega$); this corresponds to $\beta_z = 800$ for a wavelength of a. Note that because we have artificially imposed a small scale height a, the instability is stabilized at much weaker field strengths than it would be in a completely self-consistent disk. For example, in a Keplerian disk with scale height H, the instability will be present so long as the minimum unstable wavelength is less than the disk thickness, a condition which is satisfied for $\beta_z \gtrsim 1$.

2.3 *Numerical Technique*

We solve the standard equations of compressible ideal MHD (paper I, eq. [2.1]) in cylindrical coordinates through the use of finite-difference techniques. We assume infinite conductivity (flux-freezing). The numerical techniques for the hydrodynamics are essentially the same as those employed in earlier simulations of disk instabilities (Hawley 1990), except that we substitute cylindrical coordinates for the pseudo-Cartesian coordinates used in that earlier study. The basic approach is time-explicit, staggered-mesh, operator-split finite-differencing (e.g., Norman & Winkler 1986). Field evolution is handled within the framework of the constrained transport method (Evans & Hawley 1988). The constrained electromotive forces in the induction equation and the transverse $\boldsymbol{J} \times \boldsymbol{B}$ forces are constructed using information obtained along upwind Alfvén characteristics. The numerical techniques will be described in another paper (Norman et al. 1991). These MHD techniques have undergone extensive testing on a wide variety of problems (Stone et al. 1991).

The numerical mesh is divided into equally spaced zones in R of width ΔR, and equally spaced zones in z of width Δz. Several grid resolutions have been used ranging from the lowest resolution grid of 64×64 zones to the finer meshed (R, z) grid of 256 by 128 zones. We use the low resolution grid to carry out a survey of various field configurations and strengths while computing selected models at higher resolution.

One of the key diagnostics used in these simulations is a measure of the power in various Fourier components obtained by integrating over the periodic interval in z

$$f(R) = \int_0^a B_R(R, z) e^{ik_z z/a}\, dz , \tag{2.5}$$

and then averaging over radius the log of the norm of this complex-valued function

$$\frac{1}{(R_{\rm out} - R_{\rm in})} \int_{R_{\rm out}}^{R_{\rm in}} \ln|f|\, dr . \tag{2.6}$$

TABLE 1

z-FIELD SIMULATIONS: RANDOM PERTURBATION

Model	(R, z) Grid	β_z	Orbits	$\tilde{k}_z = 1$	$\tilde{k}_z = 2$	$\tilde{k}_z = 3$	$\tilde{k}_z = 4$	$\tilde{k}_z = 5$	$\tilde{k}_z = 6$
1a	64 × 64	100	2.2	...	...	...	...	...	...
1b	64 × 64	100	2.9	0.69	0.36	...	...	...	...
2a	64 × 64	1000	3.0	0.70	0.23	...	...	...	...
2b	256 × 128	1000	3.3	0.61	0.20	...	...	...	...
3a	64 × 64	4000	2.7	0.37	0.67	0.63	0.32	...	...
3b	256 × 128	4000	3.5	0.42	0.65	0.59	0.26	...	...
4a	64 × 64	16000	2.8	0.26	0.40	0.55	0.59	0.51	0.57
4b	256 × 128	16000	3.7	0.20	0.44	0.53	0.63	0.61	0.60

The radial average is carried out over the middle quarter of the grid. One can then obtain growth rates for various wavenumbers by means of a least-squares fit during the linear growth period for comparison with the linear perturbation theory of paper I. As a second diagnostic we monitor the total poloidal and toroidal magnetic energy densities on the grid as a function of time. These are obtained by direct integration over the entire domain.

As a numerical test we have run an unmagnetized, purely hydrodynamical simulation using this grid. We perturbed the initial disk by altering the angular momentum in a small region of circular cross section. As expected, the resulting ring executed characteristic epicyclic motion. Not a trace of instability was seen. But, as we show below, a very small magnetic field makes for a much different story.

3. SIMULATIONS

3.1. *Instabilities of Weak z-Fields*

We begin with a series of simulations designed to demonstrate most clearly the essential physics of the instability. Consider a pure z-field placed in a narrow region in the center of the grid, from $R - a/5$ to $R + a/5$. The intention in confining the field to a narrow radial band is to isolate the resulting dynamic evolution, and minimize the effect of the reflecting radial boundaries. As it turns out, this choice of initial field configuration has its own set of nonnegligible consequences, but these too can be isolated and understood.

We perturb the initial conditions by varying the specific enthalpy by a small, random amount (between $\pm$ 1%) in every grid zone. The resulting pressure perturbations create small random velocities. This means that all the wavenumbers available to the grid (i.e., from $2\pi/a$ down to $\pi/\Delta z$) are excited at very low amplitudes. Table 1 lists the results from a series of simulations with random initial perturbations, providing the model number, the grid resolution, the length of time to which the simulation was run, and the growth rate of the averaged Fourier component of the radial magnetic field in units of Ω for the first six z wavenumbers (eq. [2.6]).

Model 1a is a relatively strong z-field simulation with $\beta_z = 100$. The minimum unstable wavelength for this field is $\lambda_{\min} = 1.62$, larger than the periodicity length $a = 1$. Thus, there exist no unstable z wavelengths on this grid for this field strength. This model was run for 2.2 orbits. Figure 1*a* is a plot of time-dependence of the k_z ($\equiv \tilde{k}_z/2\pi$) = 1 and $\tilde{k}_z = 6$ Fourier components of the radial magnetic field. The plot shows no growth, as expected.

As a control we increase the grid size by setting $a = 3$ while retaining the same initial field of $\beta_z = 100$. The larger physical extent of the grid is the only difference between Model 1b and

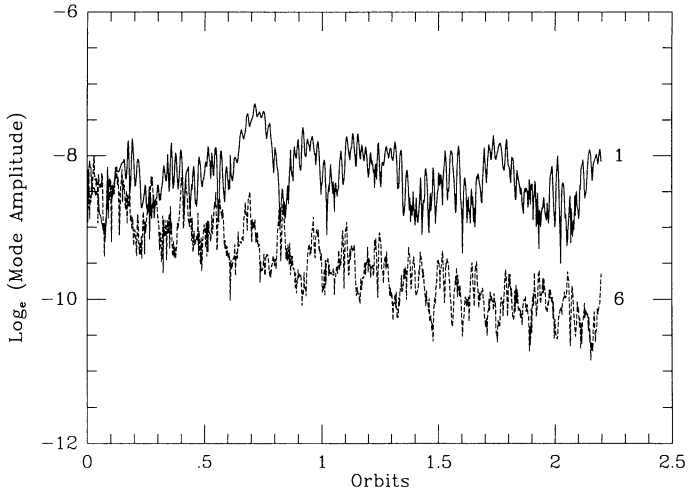

FIG. 1*a*

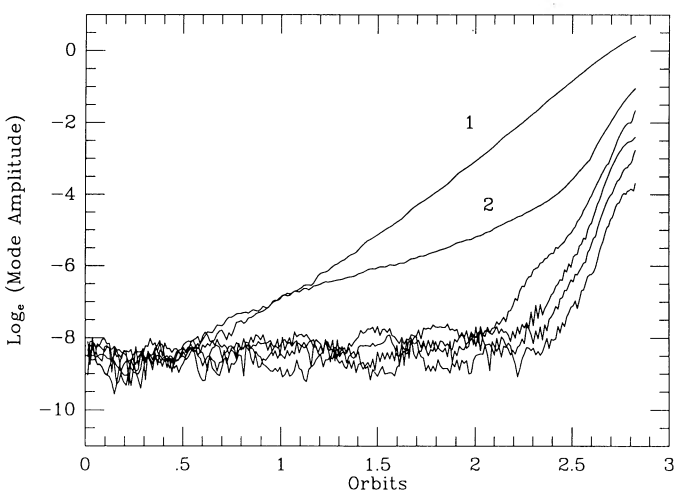

FIG. 1*b*

FIG. 1.—(*a*) Time-dependence of the $\tilde{k}_z \equiv k_z/2\pi = 1$ and $\tilde{k}_z = 6$ Fourier components of the radial magnetic field in the $\beta_z = 100$, $a = 1$ simulation (Model 1a). This model shows no mode growth. (*b*) Time-dependence of $\tilde{k}_z$ wavenumbers 1 through 6 for the $\beta_z = 100$, $a = 3$ simulation (Model 1b). Increasing the periodicity-length of the grid over that of Model 1a allows unstable modes. Wavenumbers 1 and 2 show linear growth; higher wavenumbers are linearly stable. Growth due to nonlinear mode coupling begins at 2.2 orbits.

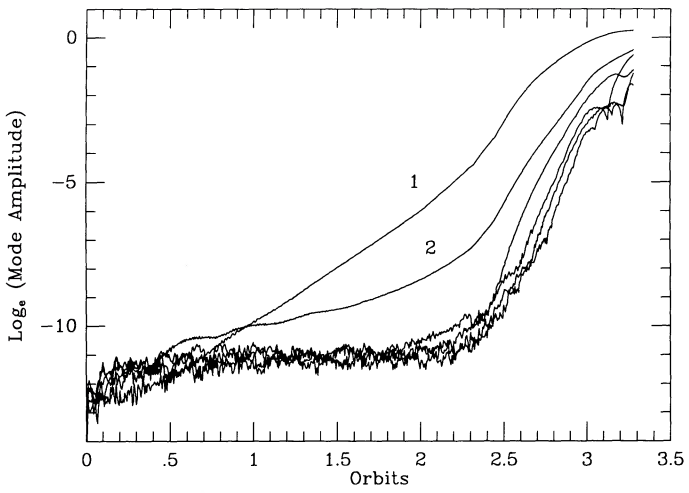

FIG. 2.—Time-dependence of $\bar{k}_z$ wavenumbers 1 through 6 for the $\beta_z = 1000$, $a = 1$ high-resolution simulation (Model 2b). As in Model 1b, only $\bar{k}_z = 1$ and 2 are unstable. However, the periodicity-length of the grid is the smaller value corresponding to that used in Model 1a. In Model 2b, the instability is enabled by decreasing the magnetic field strength.

Model 1a. In Model 1b, both the $\bar{k}_z = 1$ and $\bar{k}_z = 2$ Fourier components are growing; higher wavenumbers are not (see Fig. 1*b*). The growth rates are given in Table 1. Two things are apparent from the comparison with linear theory. First, the $\bar{k}_z = 1$ growth rate is slightly smaller than the value obtained from linear theory for a $q_z = 1$, $q_R = 0$ mode of wavelength $a = 3$. Because we have a rather restricted radial grid, it is not possible to have modes with $q_R = 0$, so it is not surprising that the growth rate should be less than the maximum pure z value. Second, a pure $\bar{k}_z = 2$ mode should be stable according to the linear analysis of paper I. As discussed in § 3.2 below, the observed growth in the $\bar{k}_z = 2$ mode is due to the choice for initial magnetic field configuration.

In Model 2 the amplitude of the magnetic field is decreased to $\beta_z = 1000$. For this field strength the minium unstable wavelength is 0.513. Figure 2 is the plot showing B_R Fourier mode amplitudes as a function of time for the high-resolution run (model 2b). The growth rate for the $\bar{k}_z = 1$ mode is 0.61. The $\bar{k}_z = 2$ mode has a growth rate of 0.19 for the first two orbits and then a growth rate of 1.26 after. This latter growth rate, equal to twice that of the $\bar{k}_z = 1$ mode, represents nonlinear mode coupling. Distinct nonlinear effects become apparent after six $\bar{k}_z = 1$ e-folding times. All the higher wavenumbers are linearly stable, although they too grow from nonlinear coupling after only 2.5 orbits.

Figure 3 consists of plots of the poloidal magnetic field lines, angular momentum, and toroidal field at the end of the simulation. It is immediately apparent that the presence of a weak magnetic field leads to a classic interchange instability. There are two regions where the angular momentum has been significantly modified. The upper blob has had its angular momentum reduced and it is moving inward (to the left) while the lower blob has had its angular momentum increased, resulting in an outward motion. Where the poloidal magnetic field has been stretched out radially, a toroidal field is generated. For these model parameters, the instability continues to grow until the field lines encounter the radial grid boundaries.

The total poloidal field energy is obtained by integrating over the numerical grid. At the beginning of the simulation this is equal to 4×10^{-9}. (Note that initially the total thermal energy $E_{\text{thermal}} = 2 \times 10^{-5}$, and the field energy is smaller than β_z times this value because the field initially occupies only a portion of the grid.) The poloidal field energy increases by a factor of 5 (to 2×10^{-8}) between orbits 2.8 and 3.3. Field energy generation proceeds during the linear growth phase through amplification of the *perturbed* field, and this becomes significant compared to the initial field energy only after large-scale motions in the fluid begin. For this model, the energy in the toroidal field is initially zero. The initial perturbations generate a small B_ϕ component giving a total energy density $\sim 10^{-15}$ after one orbit. In the remaining 2.3 orbits of the simulation the total toroidal field energy grows to 2×10^{-8}. Thus, although the field strength has grown due to the instability, its total energy remains well below the thermal energy. Nevertheless, dramatic readjustment in the structure of the disk is occurring due to the transfer of angular momentum between fluid elements.

The next two models are designed to investigate the effects of decreasing the strength of the magnetic field while holding the grid scales constant. As the magnetic field weakens the most unstable wavelengths decrease proportionally. For example, by increasing β_z to 4000 (Model 3) we reduce the minimum unstable wavelength by a factor of 2, $\lambda_{\text{min}} = 0.25$, and the fastest growing wavelength is reduced to 0.45. Model 4 with $\beta_z = 16000$ decreases these wavelengths by a further factor of 2.

Figure 4 shows the Fourier amplitudes as a function of time for Model 3b, the high-resolution, $\beta_z = 4000$ simulation. The fastest growing wavenumbers are $\bar{k}_z = 2$ and 3; $\bar{k}_z = 5$ and 6 are stable. The evolution becomes nonlinear at orbit 2, after which all modes grow at a very rapid rate. The longest wavelength model, $\bar{k}_z = 1$, is unstable with a growth rate of 0.42Ω, reduced from the value in Model 3. Nonlinear mode coupling comes into play after two orbits, after which the growth rate in the $\bar{k}_z = 1$ mode increases to 1.32Ω.

In Figure 5 we plot the poloidal field lines, the toroidal field, and the angular momentum at orbit 3.3. As with Model 2, the instability produces regions of high and low angular momentum that are moving radially through the grid. As they do so, the poloidal field lines are stretched out. A further consequence can be seen in Figure 5; X-points form in the field. Although there is no explicit finite conductivity in the numerical code, the field can numerically reconnect when there is oppositely directed field within one grid zone. This is occurring here. The resulting field loops surround regions of reduced (or increased) angular momentum. The minimum and maximum values of angular momentum present on the grid at this time correspond to Kepler orbits at $R = 97$ and 103; recall that the grids runs from $R = 99$ to 101.

Figure 6 shows the averaged Fourier amplitudes as a function of time for Model 4b, the high-resolution, $\beta_z = 16{,}000$ simulation. The slowest growing wavenumber is $\bar{k}_z = 1$; the higher wavenumbers listed in Table 1 are all unstable with rapid growth rates. After two orbits, the long wavelength $\bar{k}_z = 1$ mode grows much more rapidly due to nonlinear coupling. This is a point worth reemphasizing: although the wavelength of the most rapidly growing mode decreases with field strength, the long wavelengths remain unstable, albeit with lower growth rates. Furthermore, as seen in this simulation, nonlinear effects transfer power from short to long wavelengths as well as from long to short. Hence, even very weak fields, whose most unstable wavelengths are quite small, can create large-scale effects in the disk.

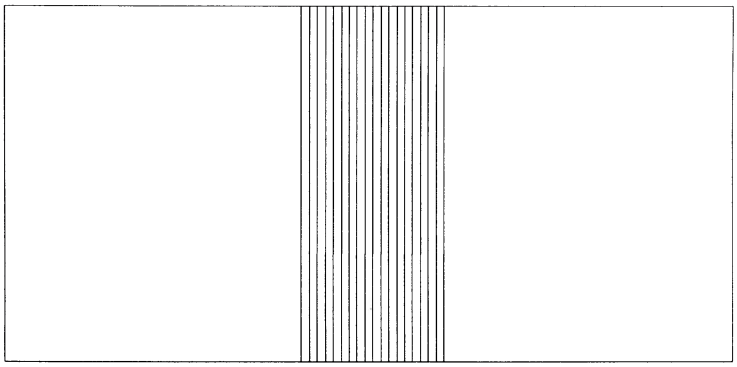

FIG. 3*a*

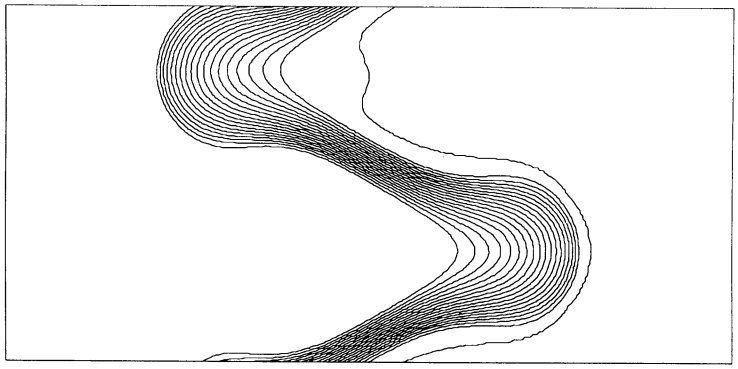

FIG. 3*b*

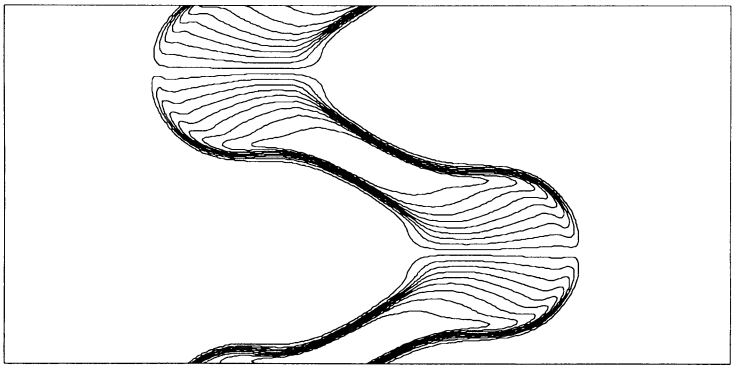

FIG. 3*c*

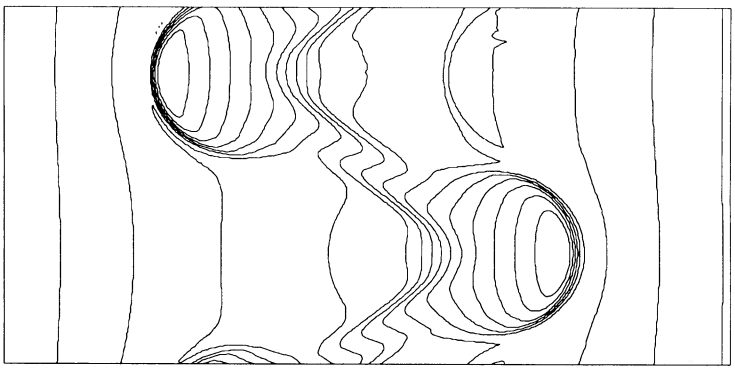

FIG. 3*d*

FIG. 3.—Contour plots of (*a*) the *initial* poloidal magnetic field lines, and (*b*) the poloidal magnetic field lines, (*c*) toroidal field, and (*d*) angular momentum at 3.3 orbits in the $\beta_z = 1000$, $a = 1$ high-resolution simulation (Model 2b). There are 20 linearly spaced contours. The angular momentum values run from 9.91 to 10.08; the Keplerian value of the angular momentum at the center of the grid is 10. The toroidal field has a maximum energy density of 2×10^{-7}.

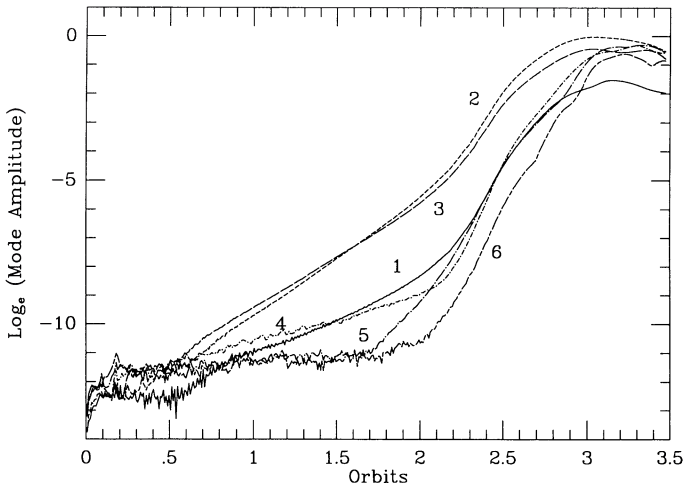

FIG. 4.—Time-dependence of $\bar{k}_z$ wavenumbers 1 through 6 for the $\beta_z = 4000$, $a = 1$ high-resolution simulation (Model 3b). The curves are labeled by their wavenumbers. Decreasing the field strength by a factor of 2 has made wavenumber 1 through 4 unstable; $\bar{k}_z = 5$ and 6 stable. Each curve is labeled by number.

Figure 7 shows the results of the instability at 3.2 orbits. The fastest growing pure z wavelength would be 0.222. On the simulation grid that wavelength is closest to $\bar{k}_z = 4$, and this is reflected in the number of large spikes and bubbles that have formed. The fastest growing wavelengths dominate through the course of the linear evolution and into the nonlinear phase. The angular momentum in the bubbles has a minimum value of 9.913, corresponding to a Kepler orbit $R_{\rm Kep} = 98$, and a maximum of 10.09 corresponding to $R_{\rm Kep} = 102$. Note that these extreme specific angular momentum values are functions only of the mode growth time, not of the strength of the magnetic field. The size of the bubbles depends on the wavelength of the unstable mode, but the specific angular momentum within that bubble, and hence the radius of its new Keplerian orbit, does not. The exchange of angular momentum between fluid elements will continue until some nonlinear effect ends it. One such effect is reconnection. As the simulations demonstrate, the radial fluid motions quickly lead to field configurations that favor such reconnection.

The random perturbations create an initial toroidal field with a total energy density of 3×10^{-16}. By the end of the simulation this has grown to 6×10^{-9}. The poloidal field begins with total energy 3×10^{-10} and peaks at 1.4×10^{-8} by orbit 3.2. The field energy then drops because of (numerical) field reconnection. The bubbles become isolated field loops and the field that defined the spikes leading to the bubbles becomes a length of (mostly) z-field near the center of the grid. At this location the angular velocity has become nearly constant with radius. Such a local angular velocity distribution can be sustained only because the grid's radial reflecting boundaries permit compensating pressure gradients.

Together, Models, 2, 3, and 4 provide a numerical demonstration of the scaling relation between mode growth and the parameter q: the growth rates of the unstable modes are independent of the field strength alone, depending only on the product of wavenumber and Alfvén speed over angular velocity. The data in Table 1 are summarized in Figure 8 where we plot growth rates as a function of q_z. Also plotted are the linear growth rate curves corresponding to several radial wavenumbers. The spread in values at a given wavenumber q_z provides an estimate of the numerical error-bars associated with both the simulation and the procedure used to obtain a growth rate. It is clear that the radial wavenumbers are not zero. In fact the modes represented here are radial averages, and must contain power from several modes of various permissible radial wavenumbers. The anomalous growth at $q_z = 1.78$ is discussed in the next section.

3.2. *The Critical Wavelength*

One obvious inconsistency between the linear stability results and the numerical simulations listed in Table 1 and plotted in Figure 8, is the observed growth for the wavenumber $q_z = 1.78$. This wavenumber is greater than the critical wavenumber $q_{\rm crit} = \sqrt{3}$, but in both Models 2 and 4 this mode is clearly unstable, albeit with a slow growth rate. In this section we describe experiments that investigate this phenomenon.

The first question to ask is, could this be a numerical effect? After all, in Model 2a the difference between the critical wavelength and the wavelength of the $\bar{k}_z = 2$ mode, $\lambda = 0.5$, is less than Δz, and the higher resolution simulations in both Model 2 and Model 3 have lower growth rates than the low resolution case. However, there is no good indication that this mode growth is simply numerical, given the range of resolutions and wavelengths tested. As one additional test of the "numerical" hypothesis we compute a 64×64 grid model with $\beta_z = 250$. For this magnetic field strength, the wavelength in question corresponds to the periodicity length of the grid, i.e., $\bar{k}_z = 1$. The results indicate that the mode grows with a rate 0.30Ω.

We consider next a physical, rather than numerical, cause. From paper I we know that the instability is due to the inability of stabilizing magnetic tension to overcome the destabilizing centrifugal force in a displacement. Any additional forces can either be stabilizing or destabilizing. In the set of simulations listed in Table 1 we consider an isolated region of magnetic field at the center of the grid. This means there will be a small magnetic pressure force directed outward from this region. The hypothesis is that this pressure acts as an additional destabilizing force and accounts for the observed growth. To test this idea, we use a new set of initial conditions with a uniform z-field throughout the grid. This will eliminate the magnetic pressure gradients due to the initial poloidal field. We run simulations on the 64×64 grid for $\beta_z = 250$, 1000, 4000, and 16000. We apply the same initial random enthalpy perturbation as were used in the simulations of Table 1. The resulting growth rates are listed in Table 2. For these simulations, no linear mode growth occurs for the $q_z = 1.78$ wavelengths. This result is consistent with our hypothesis; the additional background magnetic pressure gradient, present because of our initial conditions, acts to destabilize wavelengths near the critical value. The comparison between these two sets of simulations provides a satisfying demonstration of the balance of forces that is responsible for the critical wavelength.

3.3 *Effect of Compressibility*

The linear perturbation analysis of paper I was derived using the Boussinesq approximation, appropriate to an analysis of noncompressive waves. However, since the numerical code solves the fully compressible MHD equations, it is possible to investigate the effects of compressibility on the instability. To do this we repeat Model 2a for two different equations of state, $\gamma = 2$ and $\gamma = 4/3$. For all three equation-of-state gammas, the

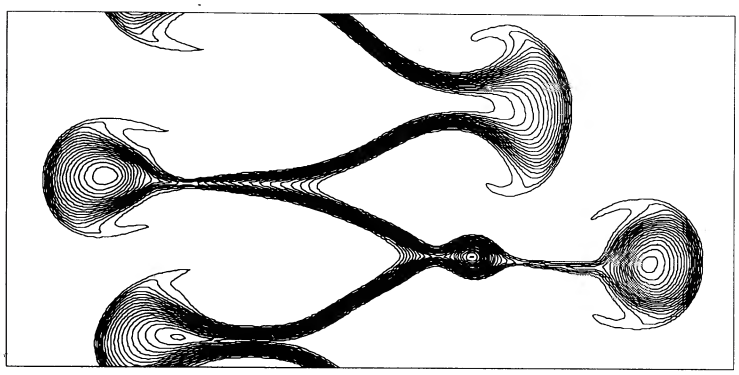

FIG. 5a

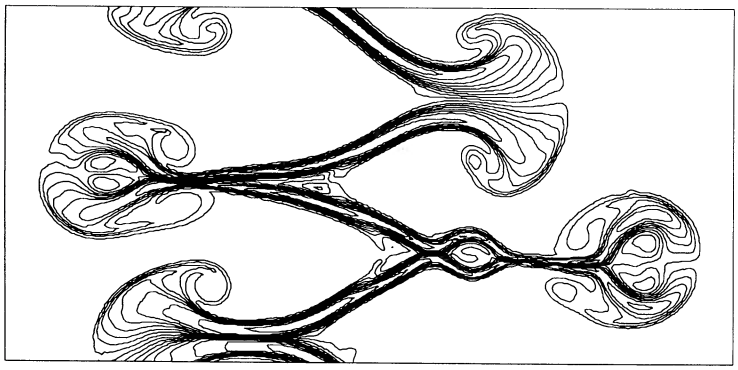

FIG. 5b

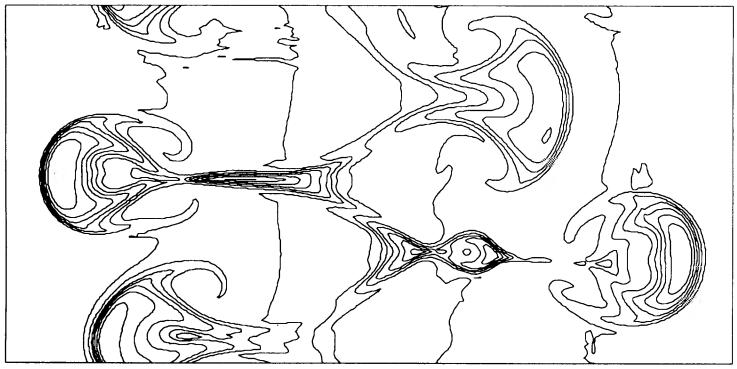

FIG. 5c

FIG. 5.—Contour plots of (*a*) the poloidal magnetic field lines, (*b*) toroidal field, and (*c*) angular momentum at 3.3 orbits in the $\beta_z = 4000$, $a = 1$ high-resolution simulation (Model 3b). There are 20 linearly spaced contours. The angular momentum values run from 9.86 to 10.14; the Keplerian value of the angular momentum at the center of the grid is 10. The toroidal field has a maximum energy density of 2×10^{-7}. At this time the z-length scale of the most prominent structures has been determined primarily by the wavelength of the fastest growing mode, $k_z = 2$.

evolution of the instability is essentially the same, as are the derived growth rates for the unstable modes. We conclude that, as anticipated, the instability is not altered by compressibility, nor by the choice of equation of state, although, as demonstrated by the experiments of § 3.2, pressure forces can play a role in determining the critical wavelength for the onset of the instability.

3.4 *Effect of Toroidal Field*

So far, all the numerical models have assumed zero initial toroidal field. The linear analysis shows that the instability and its growth rates are independent of toroidal field strength if the Boussinesq approximation holds. This will be the case so long as the toroidal field energy density is less than the thermal energy density, $\beta_\phi > 1$. As a check, we do a simulation using the parameters of Model 2a, and add a relatively strong, constant toroidal field with $\beta_\phi = 10$. (A toroidal field that is much stronger would be interesting in its own right, as it would be prone to buoyancy instabilities in a vertically stratified accretion disk.) The instability proceeds as before with the same growth rates. The main difference is that the random perturbations work with the strong toroidal field to produce larger

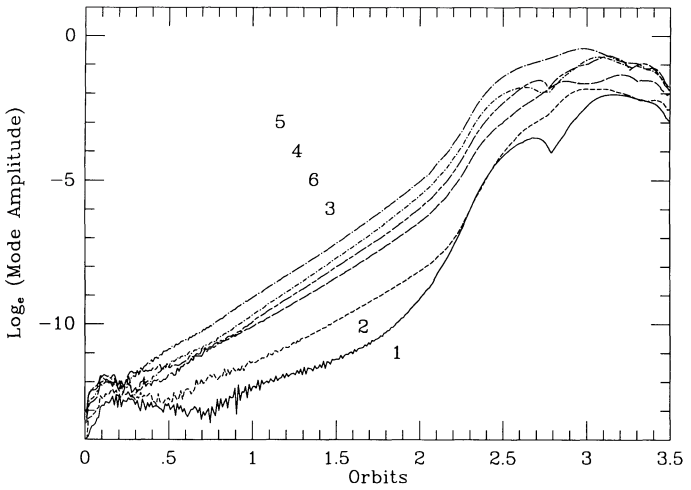

FIG. 6.—Time-dependence of k_z wavenumbers 1 through 6 for the $\beta_z = 16000$, $a = 1$ high-resolution simulation (Model 4b). All wavenumbers 1 through 6 are now unstable. The individual curves are indicated by number.

initial poloidal field perturbations. These larger initial perturbations mean that instability reaches nonlinear saturation sooner than in the otherwise equivalent Model 2a. We conclude that the instability can operate effectively even in the presence of relatively strong toroidal fields such as those expected in an accretion disk.

3.5. *Instabilities in Field Loops*

We have considered the evolution of the magnetic instability for initial configurations involving both toroidal and z-fields. Another general field topology to consider is the poloidal field loop. We observed in the earlier simulations that field loops are a likely consequence of the nonlinear evolution of a z-field. Further, one expects that field loops would be present *ab initio* in an accretion disk. We are therefore led to consider a vector potential of the form

$$A_\phi = \frac{\beta}{2} \ln\left[\frac{1}{(R - R_c)^2 + (z - z_c)^2 + 1}\right], \qquad (3.1)$$

for all $[(R - R_c)^2 + (z - z_c)^2] < r_{\rm lim}^2$, and constant otherwise, to produce circular field lines centered on (R_c, z_c) out to the limiting radius, $r_{\rm lim}$. The parameters β, $r_{\rm lim}$, and the constant in the denominator can be adjusted as desired. Here we choose $\beta = 1000$, and $r_{\rm lim} = 1/12$, and center the field loops on the 256×128 grid used in the high resolution simulations of Table 1.

Figure 9 shows the time evolution of the field. The initial configuration was randomly perturbed, as before. The final frame pictured in Figure 9 for this simulation is at 2.0 orbits. After one orbit the field loop begins to stretch out radially. Fluid elements have exchanged enough angular momentum to bring the loop out of equilibrium with it surroundings. Between 1 and 2 orbits the total poloidal field energy increases by a factor of 10 from its initial value of 10^{-10}. The toroidal field energy is zero initially, although the presence of a radial field assures linear toroidal field growth regardless of the efficacy of the instability. By two orbits the toroidal field energy has grown to 3×10^{-8}. At two orbits the minimum and maximum angular momentum values in the "mushroom caps" are 9.94 and 10.06. This simulation demonstrates that loops of poloidal field are capable of efficiently transferring angular momentum and driving the instability. The radial stretching of field loop appears to lead to a field configuration that is conducive to true dissipative reconnection.

4. CONCLUSIONS

Before summarizing our conclusions, we reiterate the various experiments done as controls and tests of the numerics. Simulations performed without magnetic fields show that the disk is hydrodynamically stable; rings that are perturbed by altering their specific angular momentum merely execute epicyclic motion. We have examined both strong and weak field configurations, and the same field strength on two grids with different periodicity lengths. This procedure tests the scaling relation between field strength and wavenumber. During that portion of the simulations for which the perturbations are small, the results are consistent with the linear perturbation theory of paper I. As discussed in § 3.2, when a uniform field is used as an initial condition (as opposed to an isolated z-field) we observe no growth for wavelengths shorter than the critical value obtained from the linear analysis. Both low- and high-resolution simulations yield the same qualitative results. In addition we have been able to test some of the limits of the linear theory. In particular we confirm that neither compressibility nor toroidal field have a significant effect on the instability.

These simulations begin to explore new territory when the unstable mode amplitudes become large. Strong mode-mode coupling can be seen in the plots of mode amplitude versus time. Both longer and shorter wavelengths can feed off power in the fastest growing mode. Although the most unstable wavelengths for very weak fields are quite small, larger wavelengths are still unstable, and the nonlinear evolution assures the growth of structure on large scales.

The most important dynamic effect is the redistribution of angular momentum. In the simulations we find that significant angular momentum is transferred between fluid elements connected by the magnetic field. This occurs on the length scales of the unstable modes. This transfer results in a strong inter-

TABLE 2

UNIFORM z-FIELD SIMULATIONS

(R, z) Grid	β_z	$k_z = 1$	$k_z = 2$	$k_z = 3$	$k_z = 4$	$k_z = 5$	$k_z = 6$
64×64.....	250	...	...	...	...	...	...
64×64.....	1000	0.63	...	...	...	...	...
64×64.....	4000	0.47	0.68	0.63	...	...	...
64×64.....	16000	0.32	0.51	0.55	0.64	0.66	0.54

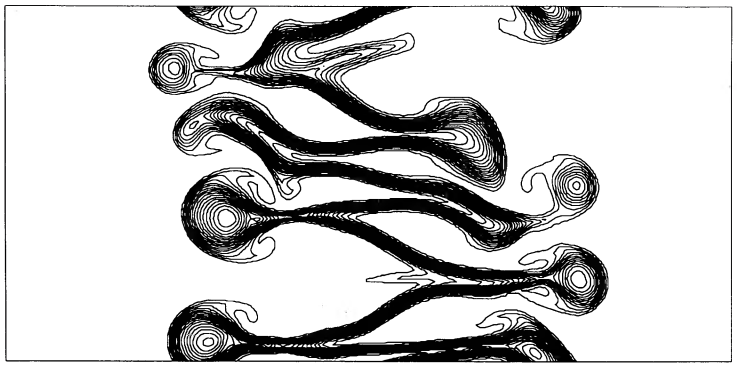

FIG. 7*a*

FIG. 7*b*

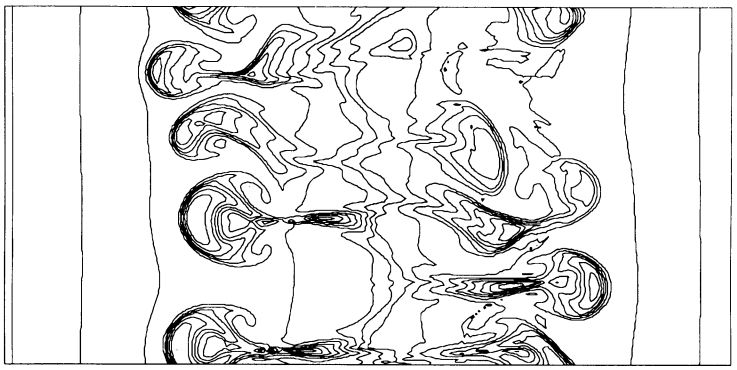

FIG. 7*c*

FIG. 7.—Contour plots of (*a*) the poloidal magnetic field lines, (*b*) toroidal field, and (*c*) angular momentum at 3.2 orbits in the $\beta_z = 16000$, $a = 1$ high-resolution simulation (Model 4b). There are 20 linearly spaced contours. The angular momentum values run from 9.91 to 10.09. The toroidal field has a maximum energy density of 2×10^{-7}.

change instability as bubbles of low or high angular momentum form and find themeselves far out of equilibrium with the surrounding gas. In all cases the angular momentum in a bubble corresponds to a Kepler orbit at a radius whose distance from the initial equilibrium location greatly exceeds the linear wavelength of the instability. Comparing simulations using field loops with those using pure z-fields indicate that the ability to transfer angular momentum is not strongly dependent on field topology. In addition, we observe that total magnetic field energy increases over the initial value by about one order of magnitude during the nonlinear growth.

How does the mode finally saturate, and how will it operate in an actual accretion disk? Because of the limited nature of the simulations presented here we can only offer suggestions. As discussed in paper I, there seem to be two possibilities: (1) the field may grow until the minimum unstable wavelength exceeds the thickness of the disk, or (2) reconnection may limit the field amplitude, leading to dissipative turbulence. The present simulations clearly favor the second possibility. The instability operates so vigorously to redistribute angular

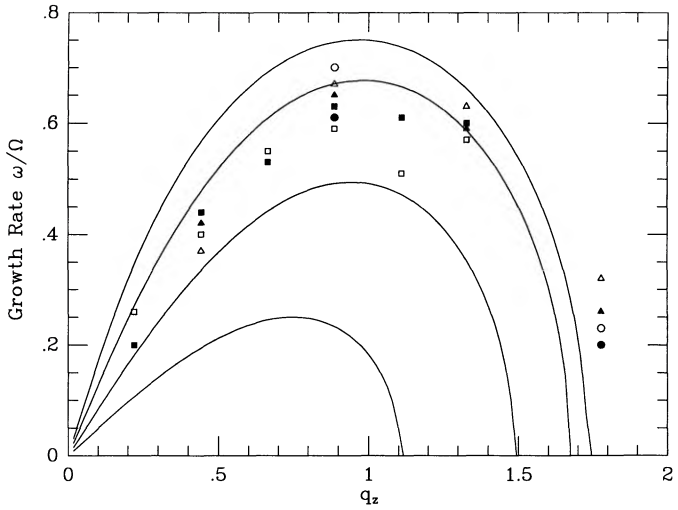

FIG. 8.—Growth rates as a function of q_z for simulations listed in Table 1. Curves represent values obtained from linear theory for $q_R = 0.$, 0.44, 0.89, and 1.33. The squares correspond to Model 4, the triangles to Model 3, and the circles to Model 2. Filled symbols represent the high-resolution simulations, open symbols represent the low.

momentum that the disk is far from equilibrium long before the initial field strength is greatly increased. Furthermore, the large radial excursions in the fluid that result from the redistribution of angular momentum, stretch out the field, providing the opportunity for field reconnection to occur. The resulting loops of poloidal field can themselves drive the instability.

Accepting that any arguments must necessarily be crude, if we adopt the turbulence picture, what is the functional dependence of the resulting viscosity? The length scale at which reconnection occurs should be roughly proportional to the most unstable wavelength, $\sim v_A/\Omega$, while typical mixing velocities should be of order this length times Ω. This suggests that

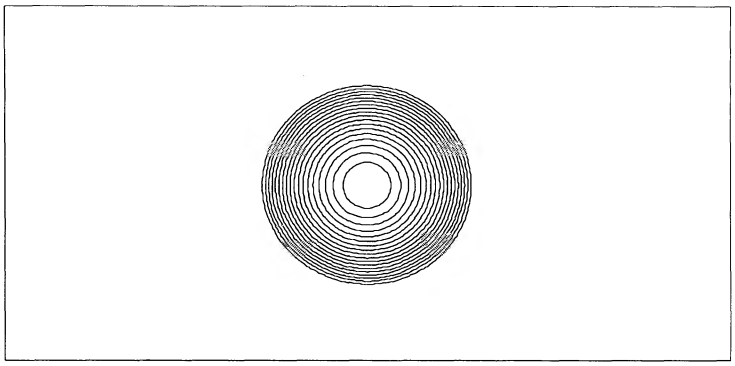

FIG. 9*a*

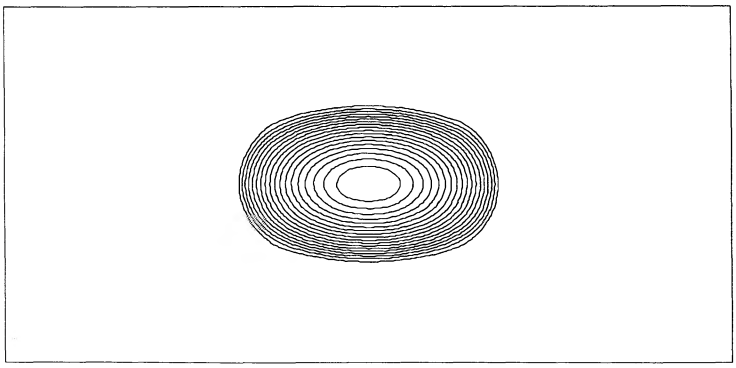

FIG. 9*b*

FIG. 9.—Poloidal magnetic field lines at (*a*) 0.4 orbits, (*b*) 0.8 orbits, (*c*) 1.2 orbits, (*d*) 1.6 orbits, and (*e*) 2.0 orbits for the evolution of a poloidal field loop. The extreme values of angular momentum in the mushroom caps at 2.0 orbits are 9.94 and 10.06, corresponding to Kepler orbits at $R = 99$ and 101.

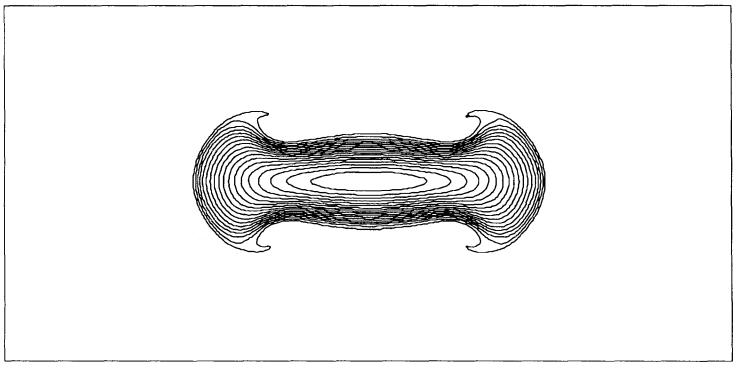

FIG. 9c

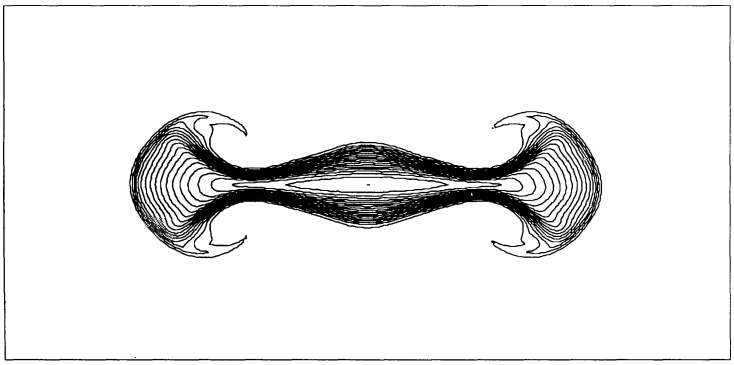

FIG. 9d

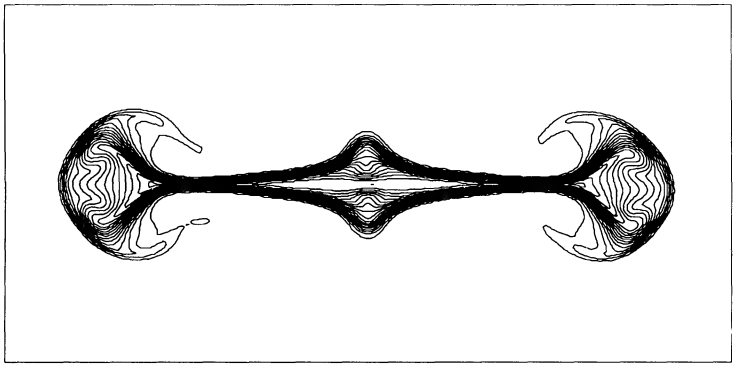

FIG. 9e

the viscosity should be $\nu \sim v_A^2/\Omega$, i.e., viscosity is a function of magnetic pressure. At this point, however, we lack a self-consistent picture of what the average magnetic field strength in a turbulent disk will be.

In both this paper and in paper I, we have shown that an initially turbulence-free Keplerian disk is dynamically unstable in the presence of a weak magnetic field. We feel that this is a very promising source of turbulence in accretion disks. In future work we will address the role of the instability in more complex initial disk models, as well as the important question of nonaxisymmetric instabilities.

This work is partially supported by NSF grants PHY-8802747 and AST-8820293, and NASA grants NAGW-1510 and NAGW-764. Computations were carried out on the Cray XMP system of the National Center for Supercomputing Applications, and the Cray YMP at the NASA Center for Computational Science.

REFERENCES

Balbus, S. A., & Hawley, J. F. 1991, ApJ, 376, 214 (I)
Evans, C. R., & Hawley, J. F. 1988, ApJ, 332, 659
Hawley, J. F., 1990, ApJ, 356, 580
Matsumoto, R., Horiuchi, T., Hanawa, T., & Shibata, K. 1990, ApJ, 356, 259
Norman, M. L., & Stone, J. M. 1990, in Galactic and Extragalactic Magnetic Fields, ed. R. Beck, P. Kronberg, & R. Wielebinski (Dordrecht: Reidel), in press
Norman, M. L., Stone, J. M., Evans, C. R., & Hawley, J. F. 1991, in preparation
Norman, M. L., & Winkler, K-H. 1986, in Astrophysical Radiation Hydrodynamics, ed. K-H. A. Winkler & M. L. Norman (Dordrecht: Reidel), p. 187
Shibata, K., & Uchida, Y. 1989, in Theory of Accretion Disks, ed. F. Meyer, et al. (Dordrecht: Kluwer), p. 65
Stone, J. M., Hawley, J. F., Norman, M. L., & Evans, C. R. 1991, in preparation